Chapter 5

Phenomenology of the Standard HVM and 95.4 GeV excess

In section 2.4 of the chapter 2, we have discussed the theoretical framework of the Standard HVM, where the flavour problem can be addressed through hierarchical vacuum expectation values (VEV) of gauge singlet scalar fields. The scalar potential emergence of the multiple ALPs scenario in the SHVM were also discussed there.

In this chapter[1], we now discuss the flavour and collider phenomenology of the Standard HVM including that of the ALPs. For investigation of the flavour phenomenology, we created `Mathematica` packages to derive the constraints on the SHVM parameters from the quark and leptonic flavour physics data. The bounds on the parameter space of the SHVM for flavour physics analysis are derived for a symmetry-conserving scalar potential, which pushes the scale Λ to several TeV. Therefore, we conduct a collider investigation of the SHVM for the scenario where the $\mathscr{Z}_N \times \mathscr{Z}_M \times \mathscr{Z}_P$ flavour symmetry of the SHVM is softly broken. This scenario can prove a rich collider phenomenology of the SHVM at the High Luminosity

[1]This chapter is based on the paper [arXiv:2412.08523 [hep-ph]], which is currently under review.

LHC (HL-LHC), the High-Energy Large Hadron Collider (HE-LHC), and a future high-luminosity 100 TeV hadron collider such as FCC-hh.

This chapter is discussed along the following track: We discuss the bounds on the SHVM from quark flavour physics in section 5.1. The bounds on the SHVM from leptonic flavour physics are presented in section 5.2. The phenomenology of the multiple ALPs is investigated in section 5.3. The collider signatures of the SHVM are presented in section 5.4.

5.1 Bounds from quark flavour physics

We first discuss the constraints arising on the masses of scalars m_{h_i} of the SHVM and the scale Λ from the quark flavour physics data in this section. The only pseudoscalar that contributes to the B_s-mixing above $\Lambda = 3 \times 10^{13}$ GeV is a_6, whose mass at this scale becomes approximately 5 GeV. However, at this scale, the contribution of the pseudoscalar a_6 is negligible to the B_s-mixing. The masses of other pseudoscalars $a_{4,5}$ remain far below the scale of any meson mixing even at the scale $\Lambda = 10^{19}$ GeV.

Among the scalars h_i, the mass of the scalar h_7 becomes approximately 5 GeV for $\Lambda = 2.5 \times 10^9$ GeV, and that of the h_1 for $\Lambda = 5.62 \times 10^5$ GeV. The Wilson coefficients of meson mixings depend on a factor of $1/\Lambda^2$ arising from the couplings of the scalars h_i with a fermion pair. This causes an extreme suppression of the Wilson coefficients making the contribution of these scalars, in particular h_7, negligible in the quark flavour physics. Therefore, the quark flavour physics does not place any bound on the mass of the scalar h_7. This observation continues to hold even for the leptonic flavour physics.

5.1.1 Neutral meson mixing

The neutral meson-antimeson mixing receives a contribution from the FCNC interactions occurring at the tree-level due to the non-diagonal couplings of the scalars h_i of the SHVM to fermions. This contribution can be incorporated by writing the following $\Delta F = 2$ effective Hamiltonian,

$$\begin{aligned}\mathscr{H}_{\rm NP}^{\Delta F=2} = {} & C_1^{ij}\,(\bar{q}_L^i\,\gamma_\mu\,q_L^j)^2 + \widetilde{C}_1^{ij}\,(\bar{q}_R^i\,\gamma_\mu\,q_R^j)^2 + C_2^{ij}\,(\bar{q}_R^i\,q_L^j)^2 + \widetilde{C}_2^{ij}\,(\bar{q}_L^i\,q_R^j)^2 \\ & + C_4^{ij}\,(\bar{q}_R^i\,q_L^j)\,(\bar{q}_L^i\,q_R^j) + C_5^{ij}\,(\bar{q}_L^i\,\gamma_\mu\,q_L^j)\,(\bar{q}_R^i\,\gamma^\mu\,q_R^j) + \text{H.c.},\end{aligned} \tag{5.1}$$

where $q_{R,L} = \frac{1\pm\gamma_5}{2}q$, and we do not show the color indices for simplicity.

The tree-level contributions of the scalars and pseudoscalars to the neutral meson mixing are given by the Wilson coefficients [147, 148],

$$\begin{aligned}C_2^{ij} &= -(y_{ji}^*)^2\left(\frac{1}{m_{h_i}^2} - \frac{1}{m_{a_i}^2}\right), \\ \tilde{C}_2^{ij} &= -y_{ij}^2\left(\frac{1}{m_{h_i}^2} - \frac{1}{m_{a_i}^2}\right), \\ C_4^{ij} &= -\frac{y_{ij}y_{ji}}{2}\left(\frac{1}{m_{h_i}^2} + \frac{1}{m_{a_i}^2}\right),\end{aligned} \tag{5.2}$$

where m_{h_i} and m_{a_i} are the masses of scalar and pseudoscalar particles of the SHVM.

The Wilson coefficients C_i are evolved from the scale Λ to scale 4.6 GeV for bottom mesons, 2.8 GeV for charmed mesons, and 2 GeV for kaons used in the lattice computations of the corresponding matrix elements [149–151]. We implement the renormalization group running of the matrix elements using the framework discussed in reference [151], and matrix elements are taken from reference [149, 150]. The numerical values of the input parameters used here are taken from the table 3.1.

The expression for the amplitudes beyond the SM for $B_q - \bar{B}_q$ and $K^0 - \bar{K}^0$ mixing have the same form as given in equations 3.3 and 3.4, respectively.

The experimental measurements of the observables of the $K^0 - \bar{K}^0$ mixing and $B_q - \bar{B}_q$ mixing are given in equations 3.5 and 3.6, where $q = s, d$, and $\mathscr{H}_{\text{eff}}^{\Delta F=2}$ shows the SM and the SHVM contributions. For future projected sensitivities of the LHCb and Belle corresponding to these observables of neutral meson mixing, we use the table 3.2.

The bounds from the neutral meson mixing in general depend on the product of couplings $y_{ij}\varepsilon_i y_{ji}\varepsilon_j / v_i v_j$ appearing in the corresponding Wilson coefficients, which can also be written in terms of the parameter Λ. Therefore, if the the product $y_{ij}\varepsilon_i y_{ji}\varepsilon_j$ is smaller, a contribution of the corresponding Wilson coefficients can be easily accommodated. Alternatively, a large value of the VEVs can make the contribution of the Wilson coefficients sufficiently small to accommodate within the experimental bounds. Therefore, the bounds from meson mixing on the parameter space of the SHVM in terms of the masses of the scalars h_i and the scale Λ become stronger as the value of the parameter ε_i increases.

In figure 5.1, we show bounds on the parameter space of the SHVM in terms of the masses of the scalars h_i and the scale Λ for $\lambda_\chi = 1$. The solid continuous straight lines, in general, show allowed parameter space, and dashed discontinuous lines are for excluded parameter space. We note that the bounds show a linear behavior in the $m_{h_i} - \Lambda$ plane, and the allowed parameter space is along the straight lines corresponding to different masses of scalars h_i. The bounds from the observable C_{ε_K} are more stringent than those of the observable $C_{\Delta m_K}$. As discussed earlier, the mass of the scalar h_7 remains unconstrained. The bounds from the observable $C_{\Delta m_K}$ for the future projected sensitivity of the neutral kaon mixing show a slight change in comparison to the bounds given in figure 5.1a. We show the effect of

the variation of the quartic coupling λ_χ on the bounds from the observable C_{ε_K} in figure 5.2. However, we use $\lambda_\chi = 1$ in our phenomenological investigations.

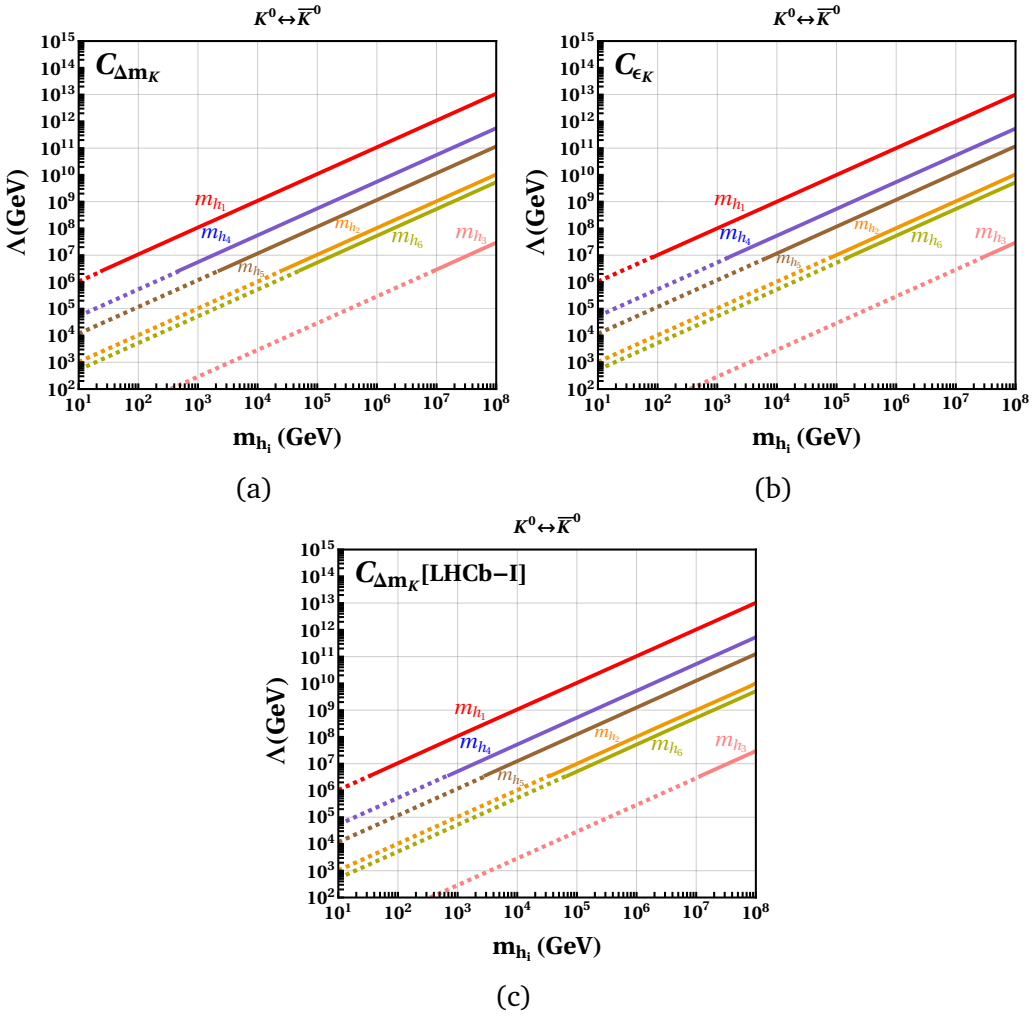

(a) (b) (c)

Fig. 5.1 Constraints on the masses of the scalars m_{h_i} and the scale Λ from the experimental measurements of the observables of neutral-kaon oscillations, assuming the quartic coupling $\lambda_\chi = 2$. The solid lines represent the allowed regions, while the dashed lines indicate the excluded parameter space. Figure 5.1a shows the bounds on the scalar masses m_{h_i} and the scale Λ from $C_{\Delta m_K}$. Figure 5.1b represents the constraints from the observable C_{ε_K}, and Figure 5.1c depicts the parameter space allowed by the projected sensitivity of $C_{\Delta m_K}$ in LHCb Phase-I.

The bounds on the parameter space of the SHVM from the neutral B_s meson mixing are shown in figure 5.3. In this case, the bounds from the observable C_{B_s} and that of the observable $\phi^o_{B_s}$ are very similar. Therefore, we show the bounds only

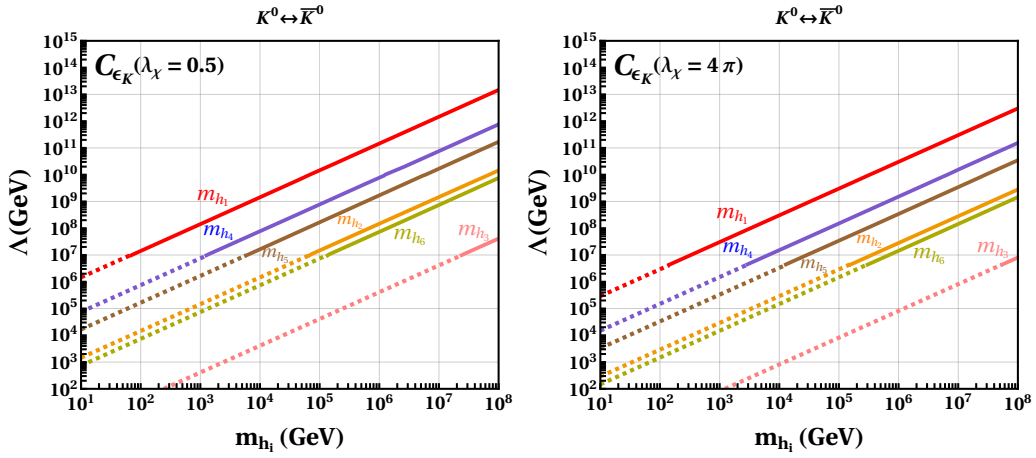

(a) (b)

Fig. 5.2 Constraints on the masses of the scalars m_{h_i} and the scale Λ from the observable C_{ε_K}, for varying values of the quartic coupling λ_χ. In figure 5.2a, we show the bounds corresponding to quartic coupling $\lambda_\chi = 0.5$, while figure 5.2b represents the bounds for $\lambda_\chi = 4\pi$. The solid lines represent the allowed regions, while the dashed lines indicate the excluded parameter space.

from the observable C_{B_s} in figure 5.3a. The bounds on the parameter space of the SHVM from the future projected sensitivity of the LHCb-II of the neutral B_s meson mixing are depicted in figure 5.3b. We notice that the neutral B_s meson mixing is not capable of constraining the mass of the scalar h_1.

In the case of the neutral B_d meson mixing shown in figure 5.4, the observables C_{B_d} and $\phi^o_{B_d}$ provide similar bounds. Therefore, only the bounds from the observable C_{B_d} are shown in figure 5.4a. We show the bounds from the future projected sensitivity of the LHCb-II of the neutral B_d meson mixing in figure 5.4b. The neutral B_d meson mixing does not constrain the mass of the scalar h_1.

Now we discuss crucial distinct features of the SHVM. In the case of neutral kaon, B_s and B_d mixings, the contribution of pseudoscalars $a_{4,5,6}$ is practically zero to the mixing observables. This is because the masses of the pseudoscalars $a_{4,5}$ are far below the scale of the meson mixing even at the scale $\Lambda = 2 \times 10^{16}$ GeV. The pseudoscalars $a_{5,6}$ become heavy above the scale $\Lambda = 2 \times 10^{16}$ GeV. However,

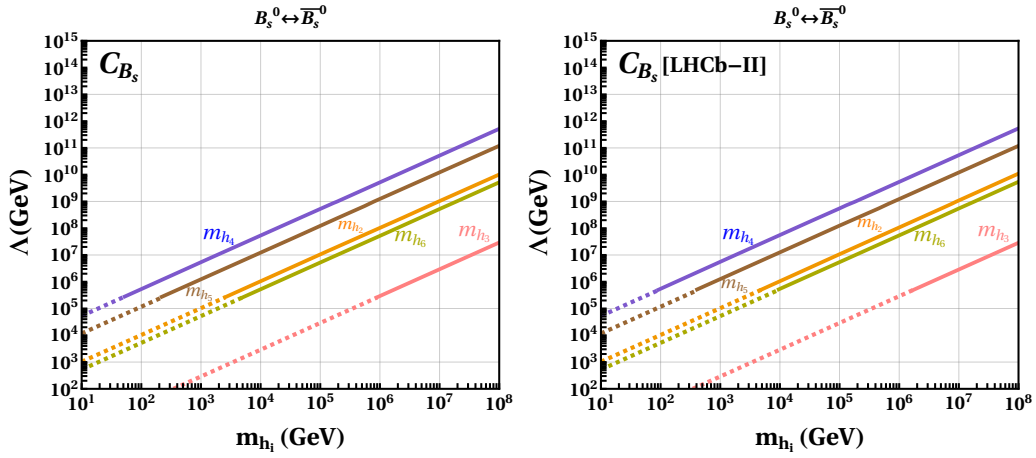

(a) (b)

Fig. 5.3 Constraints on the masses of the scalars m_{h_i} and the scale Λ from the observables of neutral-B_s meson mixing $B_s^0 - \bar{B}_s^0$, assuming the quartic coupling $\lambda_\chi = 2$. Figure 5.3a shows the bounds on the scalar masses m_{h_i} and the scale Λ from the current measurement of C_{B_s}, while Figure 5.3b depicts the constraints by the projected sensitivity of C_{B_s} in LHCb Phase-II. The solid lines represent the allowed regions, while the dashed lines indicate the excluded parameter space.

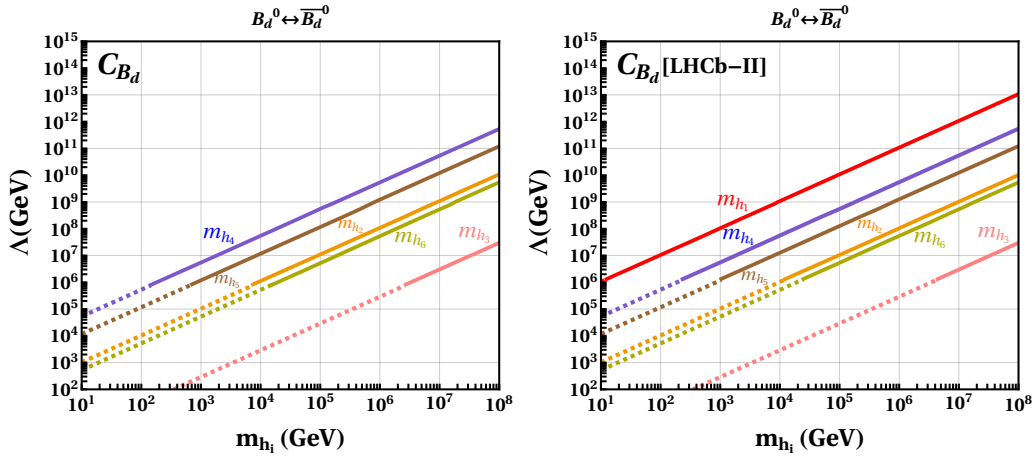

(a) (b)

Fig. 5.4 Constraints on the masses of the scalars m_{h_i} and the scale Λ from the observables of neutral-B_d meson mixing $B_d^0 - \bar{B}_d^0$, assuming the quartic coupling $\lambda_\chi = 2$. Figure 5.4a shows the bounds on the scalar masses m_{h_i} and the scale Λ from the current measurement of C_{B_d}, while Figure 5.4b depicts the constraints by the projected sensitivity of C_{B_d} in LHCb Phase-II. The solid lines represent the allowed regions, while the dashed lines indicate the excluded parameter space.

the scale $\Lambda = 2 \times 10^{16}$ GeV causes a huge amount of the suppression of the Wilson coefficients resulting in practically zero contribution to the meson mixing. This is a distinct feature of the SHVM. This observation continues to hold even for the leptonic decays of mesons and the leptonic flavour physics. Therefore, we can conclude that the pseudoscalars a_i practically do not contribute to the quark and leptonic physics.

A more striking observation is the neutral D-meson mixing. The SHVM does not predict any deviation in the neutral D-meson mixing over its SM prediction. This is due to the absence of the required couplings of the scalars and pseudoscalars for the neutral D-meson mixing. This keeps apart the SHVM from the other models of flavour, based on extended Higgs sector, for instance see reference [230].

5.1.2 Leptonic decays of mesons

The effective Hamiltonian for a pseudoscalar meson decaying into two charged leptons is,

$$\mathscr{H}_{\text{eff}} = -\frac{G_F^2 m_W^2}{\pi^2}\left(C_S^{ij}(\bar{q}_i P_L q_j)\bar{\ell}\ell + \tilde{C}_S^{ij}(\bar{q}_i P_R q_j)\bar{\ell}\ell + C_P^{ij}(\bar{q}_i P_L q_j)\bar{\ell}\gamma_5\ell + \tilde{C}_P^{ij}(\bar{q}_i P_R q_j)\bar{\ell}\gamma_5\ell\right) + \text{H.c.}. \tag{5.3}$$

The branching ratio is given by,

$$\begin{aligned}\text{BR}(M \to \ell^+\ell^-) = &\frac{G_F^4 m_W^4}{8\pi^5}\beta\, m_M f_M^2 m_\ell^2 \tau_M \\ &\left(\left|\frac{m_M^2\left(C_P^{ij} - \tilde{C}_P^{ij}\right)}{2m_\ell(m_i+m_j)} - C_A^{\text{SM}}\right|^2 + \left|\frac{m_M^2\left(C_S^{ij} - \tilde{C}_S^{ij}\right)}{2m_\ell(m_i+m_j)}\right|^2 \beta^2\right),\end{aligned} \tag{5.4}$$

where $\beta(x) = \sqrt{1-4x^2}$ and $x = m_\ell/m_M$.

The Wilson coefficients parameterizing the tree-level contribution of the scalars and pseudoscalars of the SHVM are [147, 148],

$$\begin{aligned} C_S^{ij} &= \frac{\pi^2}{2G_F^2 m_W^2}\frac{2y_{\ell\ell}y_{ji}}{m_{h_i}^2}, \\ \tilde{C}_S^{ij} &= \frac{\pi^2}{2G_F^2 m_W^2}\frac{2y_{\ell\ell}y_{ij}}{m_{h_i}^2}, \\ C_P^{ij} &= \frac{\pi^2}{2G_F^2 m_W^2}\frac{2y_{\ell\ell}y_{ji}}{m_{a_i}^2}, \\ \tilde{C}_P^{ij} &= \frac{\pi^2}{2G_F^2 m_W^2}\frac{2y_{\ell\ell}y_{ij}}{m_{a_i}^2}. \end{aligned} \tag{5.5}$$

The one-loop SM contribution to the two-body leptonic decays of a pseudoscalar meson into two charged leptons is given by [148],

$$C_A^{\mathrm{SM}} = -V_{tb}^* V_{ts}\, Y\left(\frac{m_t^2}{m_W^2}\right) - V_{cb}^* V_{cs}\, Y\left(\frac{m_c^2}{m_W^2}\right), \tag{5.6}$$

where $Y(x)$ is the Inami-Lim function, given by [162],

$$Y(x) = \eta_{\mathrm{QCD}}\frac{x}{8}\left[\frac{4-x}{1-x} + \frac{3x}{(1-x)^2}\log x\right], \tag{5.7}$$

where $\eta_{\mathrm{QCD}} = 1.0113$ denotes the NLO QCD effects [163]. For B_d meson, we can obtain the SM predictions by replacing the indices in equation 5.6.

The $B_{s,d}$ meson decays

The experimental values of the branching fractions for the decays of neutral B_s and B_d meson to muon pairs are taken from the equations 3.14 and 3.15, respectively.

The theoretical branching fraction of the B_s meson is multiplied by the factor $(1-y_s)^{-1}$ to relate it to the experimental branching ratio [167], where $y_s = 0.088 \pm$

0.014 [168]. This will account for the sizeable width difference of the B_s meson, and can be neglected in the case of B_d meson.

We show the bounds on the parameter space of the SHVM from the BR($B_d \to \mu^+\mu^-$) and BR($B_s \to \mu^+\mu^-$) branching fractions in figure 5.5. The BR($B_s \to \mu^+\mu^-$) branching fraction provides slightly constrained bounds over that of the BR($B_d \to \mu^+\mu^-$) branching ratio.

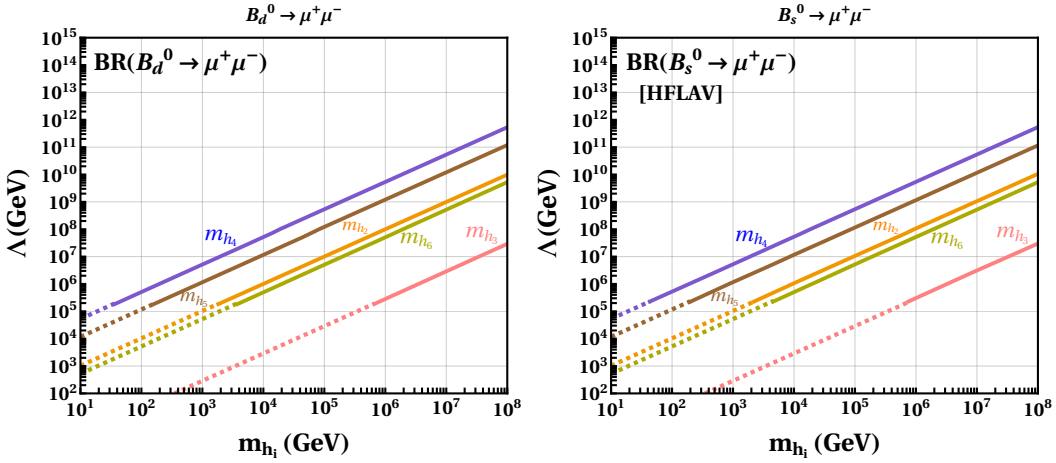

(a) (b)

Fig. 5.5 Constraints on the masses of the scalars m_{h_i} and the scale Λ from $B_{s,d}$ meson decays to muon pairs, assuming the quartic coupling $\lambda_\chi = 2$. Figure 5.5a shows the bounds from the measurement of BR($B_d \to \mu^+\mu^-$), while Figure 5.5b depicts the constraints by the BR($B_s \to \mu^+\mu^-$). The solid lines represent the allowed regions, while the dashed lines indicate the excluded parameter space.

The ratio of the BR($B_d \to \mu^+\mu^-$) and BR($B_s \to \mu^+\mu^-$) branching fractions, $\mathscr{R}_{\mu\mu}$, can also be used to constrain the parameter space of the SHVM. This is measured by the LHCb, and is given in equation 3.16.

The measured average value of the effective lifetime $\tau_{\mu\mu}$ discussed in equations 3.19 and 3.23 can also be used to constrain the parameter space of the SHVM.

We also utilize the current and future sensitivities of the observables $B_s \to \mu^+\mu^-$, the ratio $\mathscr{R}_{\mu\mu}$, and the effective lifetime $\tau_{\mu\mu}$, given in the table 3.3.

The bounds from the observable $\mathscr{R}_{\mu\mu}$ are shown in figure 5.6. The current measurement of the ratio $\mathscr{R}_{\mu\mu}$ provides the most relaxed bounds among the quark observables, which is shown in figure 5.6a. In figure 5.6b, we show the bounds from the future projected sensitivities of the ratio $\mathscr{R}_{\mu\mu}$ in the phases LHCb-I and LHCb-II. The allowed parameter space for the high luminosity phase of the LHCb-II is superimposed on that of the phase of the LHCb-I, and is shown in black. We notice that phase LHCb-II measurement of the observable $\mathscr{R}_{\mu\mu}$ will provide the most powerful bounds on the parameter space of the SHVM. The bounds on the parameter space of the SHVM from the effective lifetime $\tau_{\mu\mu}$ are shown in figure 5.7.

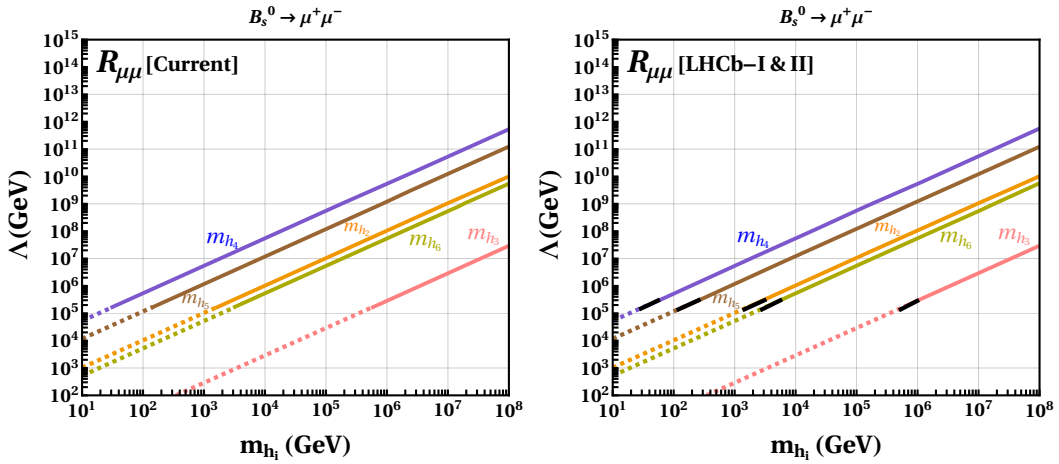

(a) (b)

Fig. 5.6 Figure 5.6a shows the constraints on the masses of the scalars m_{h_i} and the scale Λ from current measurement of the observable $\mathscr{R}_{\mu\mu}$. Figure 5.6b depicts the constraints from the future projected sensitivities of the ratio $\mathscr{R}_{\mu\mu}$ in the high-luminosity phases LHCb-I and LHCb-II, where, in particular, the black colored lines, which are superimposed on that of the solid colored lines of phase LHCb-I, show the allowed parameter space for LHCb-II. The dashed lines indicate the excluded parameter space, and we have assumed the quartic coupling $\lambda_\chi = 2$.

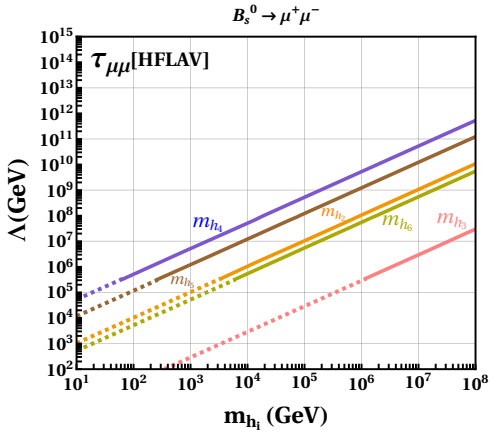

Fig. 5.7 Constraints on the masses of the scalars m_{h_i} and the scale Λ from current measurement of the effective lifetime $\tau_{\mu\mu}$, assuming the quartic coupling $\lambda_\chi = 2$. The solid lines represent the allowed regions, while the dashed lines indicate the excluded parameter space.

The K_L meson decays

The SM contribution of the $K_L \to \mu^+\mu^-$ decay is discussed in the equation 3.24. To constrain the parameter space of the SHVM, we use the upper limit of the short-distance contribution of $K_L \to \mu^+\mu^-$ decay extracted from the experimental measurement, as given in the equation 3.25. We show the bounds on the parameter

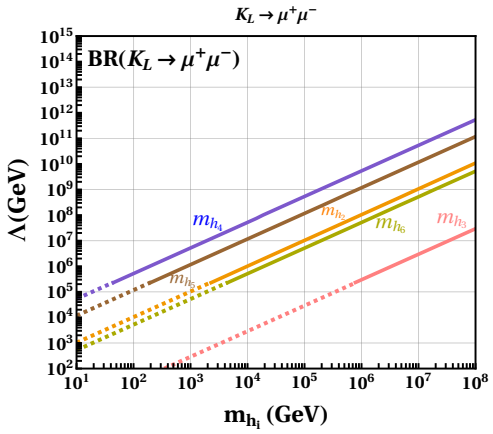

Fig. 5.8 Constraints on the masses of the scalars m_{h_i} and the scale Λ from the experimental upper limits of BR$(K_L \to \mu^+\mu^-)_{\rm SD}$, assuming the quartic coupling $\lambda_\chi = 2$. The solid lines represent the allowed regions, while the dashed lines indicate the excluded parameter space.

space of the SHVM from the $K_L \to \mu^+\mu^-$ decay in figure 5.8.

5.2 Bounds from lepton flavour physics

The charged lepton flavour violation (CLFV) processes place stringent bounds on the parameter space of the SHVM. To derive the constraints on the parameter space of the SHVM, we utilize the experimental upper limits on various leptonic flavour violation processes, as given in table 3.4.

5.2.1 Radiative leptonic decays

The effective Lagrangian for the radiative leptonic decays can be written as,

$$\mathscr{L}_{\text{eff}} = m_{\ell'} C_T^L \bar{\ell} \sigma^{\rho\lambda} P_L \ell' F_{\rho\lambda} + m_{\ell'} C_T^R \bar{\ell} \sigma^{\rho\lambda} P_R \ell' F_{\rho\lambda}. \tag{5.8}$$

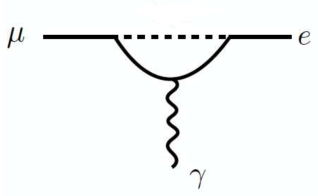

Fig. 5.9 Feynman diagram representing $\mu \to e\gamma$ decay, where dashed line shows the contributions of scalars (h_i) and pseudoscalars (a_i) of the SHVM.

The branching ratio of the radiative leptonic decays turns out to be,

$$\text{BR}(\ell' \to \ell\gamma) = \frac{m_{\ell'}^5}{4\pi\Gamma_{\ell'}} \left(|C_T^L|^2 + |C_T^R|^2 \right). \tag{5.9}$$

We show the one-loop contribution to radiative leptonic decays in figure 5.9. The one-loop contribution can be parametrized in terms of the following Wilson

coefficients [102],

$$C_T^L = (C_T^R)^* = \frac{e}{32\pi^2}\sum_{k=e,\mu,\tau}\left\{\frac{1}{6}\left(y^*_{\ell k}y_{\ell' k}+\frac{m_\ell}{m_k}y^*_{k\ell}y_{k\ell'}\right)\left(\frac{1}{m^2_{h_i}}-\frac{1}{m^2_{a_i}}\right)\right.$$
$$\left.-\,y_{\ell k}y_{k\ell'}\frac{m_k}{m_{\ell'}}\left[\frac{1}{m^2_{h_i}}\left(\frac{3}{2}+\log\frac{m^2_{\ell'}}{m^2_{h_i}}\right)-\frac{1}{m^2_{a_i}}\left(\frac{3}{2}+\log\frac{m^2_{\ell'}}{m^2_{a_i}}\right)\right]\right\}. \tag{5.10}$$

The bounds from the branching ratio of the radiative leptonic decays are shown in figure 5.10. On the left, we show the bounds from the current measurement of the MEG experiment, and on the right, bounds from the future MEG-II experiment are shown.

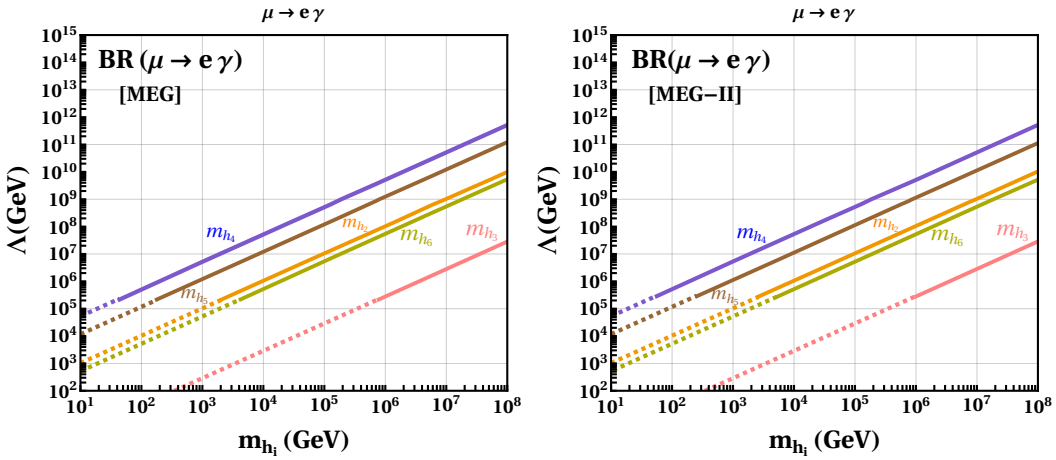

(a) (b)

Fig. 5.10 Constraints on the masses of the scalars m_{h_i} and the scale Λ from the experimental upper limits of radiative leptonic decay $\mu \to e\gamma$, as given in the table 3.4, assuming the quartic coupling $\lambda_\chi = 2$. Figure 5.10a shows the bounds from limits on the observable BR($\mu \to e\gamma$) by MEG, and Figure 5.10b depicts the constraints from the projected sensitivity of BR($\mu \to e\gamma$) by MEG-II. The solid lines represent the allowed regions, while the dashed lines indicate the excluded parameter space.

5.2.2 $A\ \mu \to A\ e$ conversion

The effective Lagrangian describing the $A\ \mu \to A\ e$ conversion is given by,

$$\mathscr{L}_{\text{eff}} = C_{qq}^{VL}\,\bar{e}\gamma^{\nu}P_L\mu\,\bar{q}\gamma_{\nu}q + m_{\mu}m_q C_{qq}^{SL}\bar{e}P_R\mu\,\bar{q}q + m_{\mu}\alpha_s C_{gg}^{L}\,\bar{e}P_R\mu\,G_{\rho\nu}G^{\rho\nu} + (R \leftrightarrow L), \tag{5.11}$$

There is also an additional contribution to $A\ \mu \to A\ e$ conversion from the dipole operators given in equation (5.8). The Feynman diagrams for $A\ \mu \to A\ e$ conversion are shown in figure 5.11, and the corresponding Wilson coefficients for the Feynman diagram on the left in figure 5.11 are written as [102],

$$\begin{aligned} C_{qq}^{SL} &= \left(\frac{1}{m_{h_i}^2} + \frac{1}{m_{a_i}^2}\right) y_{\mu e}^{*}\text{Re}(y_{qq})\,, \\ C_{qq}^{SR} &= \left(\frac{1}{m_{h_i}^2} - \frac{1}{m_{a_i}^2}\right) y_{e\mu}\text{Re}(y_{qq})\,. \end{aligned} \tag{5.12}$$

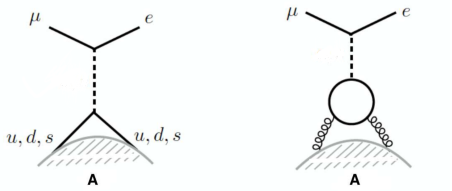

Fig. 5.11 Feynman diagram showing $A\ \mu \to A\ e$ conversion, where dashed lines represent the scalars (h_i) and pseudoscalars (a_i) of the SHVM.

We can include the nuclear effects of quarks inside the nucleons as well as the contribution of the Feynman diagram on the right side of figure 5.11 by writing the nucleon-level Wilson coefficients, in the same form as discussed in equation 3.32. Similar to previous case, we ignore the vector operators due to their negligible contribution [102]. The numerical values of the vector and scalar couplings are taken from equation 3.33.

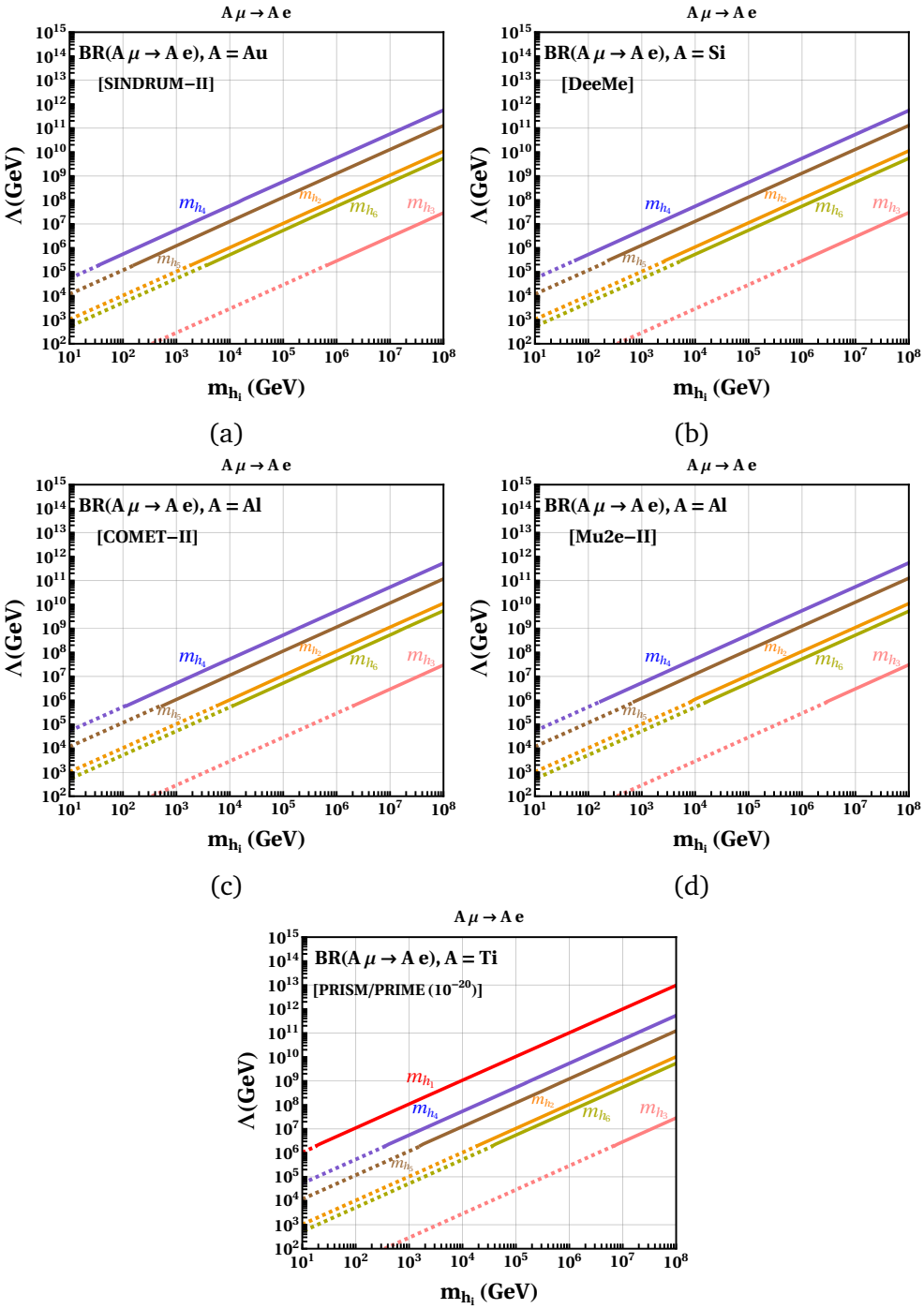

Fig. 5.12 In figures 5.12a, 5.12b, 5.12c, 5.12d, and 5.12e, we show constraints on the masses of the scalars m_{h_i} and the scale Λ from the experimental upper limits on BR$(A\mu \to Ae)$ by the current as well as projected sensitivities of the various experiments given in the table 3.4, assuming the quartic coupling $\lambda_\chi = 2$. The solid lines represent the allowed regions, while the dashed lines indicate the excluded parameter space.

The $A\ \mu \to A\ e$ conversion rate can be written as [102],

$$\Gamma_{A\ \mu\to A\ e} = \frac{m_\mu^5}{4}\left|C_T^L D + 4\left[m_\mu m_p \tilde{C}_p^{SL} + \tilde{C}_p^{VL} V^p + (p\to n)\right]\right|^2 + L \to R, \tag{5.13}$$

where the nuclear effects are included. The numerical values of the dimensionless coefficients $D, S^{p,n}$, and $V^{p,n}$ are taken from the table 3.5.

We show bounds from the $A\ \mu \to A\ e$ conversion rate for the present and future sensitivities of different experiments in figure 5.12. It turns out that the future sensitivities of the $A\ \mu \to A\ e$ conversion rate can provide stringent constraints on the SHVM parameter space.

5.2.3 The $\mu \to 3e$ and $\tau \to 3\mu$ decays

The three body flavour violating leptonic decays $\mu \to 3e$ and $\tau \to 3\ell$ ($\ell = e, \mu$) are additional sources to probe the dipole operators given in equation (5.8). The decay rate can be written as [102],

$$\Gamma(\ell' \to 3\ell) = \frac{\alpha m_\ell'^5}{12\pi^2}\left|log\frac{m_\ell'^2}{m_\ell^2} - \frac{11}{4}\right|\left(|C_T^L|^2 + |C_T^R|^2\right). \tag{5.14}$$

where the tree-level contribution can be ignored due to the strong chiral-suppression caused by the logarithmic enhancement of the dipole operators[102]. The other contributions, such as Z-mediated penguin, are negligible due to their strong suppression [193].

The bounds on the parameter space of the SHVM from the $\mu \to 3e$ decay are shown in figure 5.13. We notice that the bounds for the Mu3e experiments are relatively stronger. The bounds from the $\tau \to 3\mu$ decays are weaker than that of $\mu \to 3e$ decays. Therefore, we do not show them in this work.

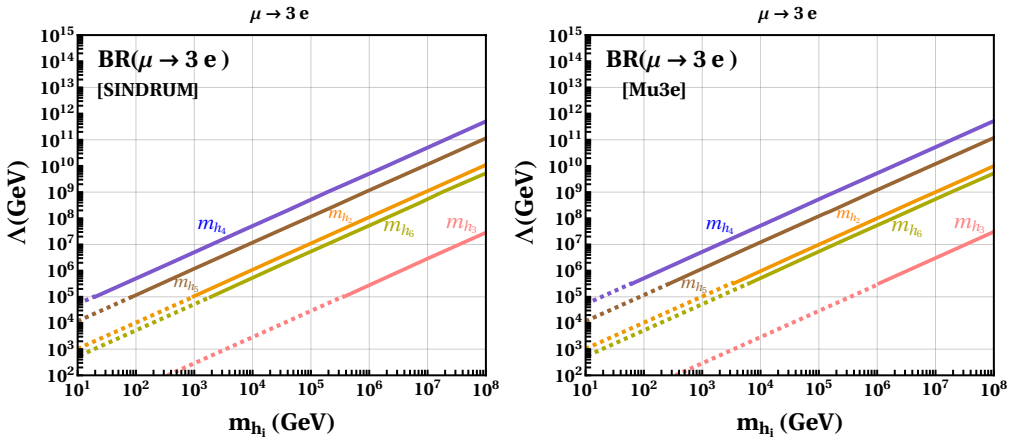

(a) (b)

Fig. 5.13 In figures 5.13a and 5.13b, we show constraints on the masses of the scalars m_{h_i} and the scale Λ from the experimental upper limits on BR$(\mu \to 3e)$ by the sensitivities of the experiments SINDRUM and Mu3e, respectively, as given in the table 3.4, assuming the quartic coupling $\lambda_\chi = 2$. The solid lines represent the allowed regions, while the dashed lines indicate the excluded parameter space.

5.3 Phenomenology of multiple ALPs

Most of the axial degrees of freedom of the gauge singlet fields χ_i and χ_7 are light , and are the source of the flavour changing neutral current processes [231]. We notice that in the standard HVM, the generic $\mathscr{Z}_2 \times \mathscr{Z}_M \times \mathscr{Z}_{14}$ flavour symmetry enforces a $U(1)$ symmetry in the Yukawa Lagrangian. The fermions transform as $\psi^f_{L/R,i} \to \exp(ix^f_i a_i/v_i)\psi^f_{L/R,i}$ for $f = q,u,d,l,e$ under $U(1)$ symmetry. The parameters ε_i are assigned $+1$ of the $U(1)$ symmetry, and the charge of the parameter ε_7 is 0. Thus, the field χ_7 is a singlet of the enforced $U(1)$ symmetry.

The fermion fields $\psi^q_{L,i}$, $\psi^u_{R,i}$, $\psi^d_{R,i}$, $\psi^l_{L,i}$, and $\psi^l_{R,i}$ have the following charges under $U(1)$ symmetry:

$$x^q_i = (1,1,1),\ x^u_i = (0,0,0),\ x^d_i = (0,0,0),\ x^l_i = (1,1,1),\ \text{and}\ x^e_i = (0,0,0), \quad (5.15)$$

We assume that the mass of the vector gauge boson corresponding to the local $U(1)$ symmetry is much heavier than the masses of all ALPs. The $U(1)$ symmetry induces the derivative couplings of the axial boson a_i:

$$-\mathscr{L}_{a_i} = \frac{\partial_\mu a_i}{v_i} \sum_{f,i} x_i^f \, \bar{\psi}^f_{L/R,i} \gamma^\mu \psi^f_{L/R,i}. \tag{5.16}$$

After diagonalizing the charged fermion mass matrices through bi-unitary transformations, we have the following FCNC Lagrangian,

$$-\mathscr{L}_{a_i} = \frac{\partial_\mu a_i}{v_i} \sum_{f=u,d,e} \bar{f}_i \left(\gamma^\mu V^f_{ij} - \gamma^\mu \gamma_5 A^f_{ij} \right) f_j, \tag{5.17}$$

where $V^f/A^f = X^f_L \pm X^f_R$ with $X^{u,d}_L = U^\dagger_{u,d} x^q U_{u,d}$, $X^{u,d}_R = V^\dagger_{u,d} x^{u,d} V_{u,d}$, and $X^e_L = U^\dagger_e x^l U_e$, $X^e_R = V^\dagger_e x^e V_e$.

The coupling of the ALPs a_i to a pair of photons can be used to observe the ALPs a_i, and can be given by,

$$\mathscr{L}^{a_i\gamma\gamma}_{\text{eff}} = \frac{1}{4} g_{a_i\gamma\gamma} \varphi F^{\mu\nu} \tilde{F}_{\mu\nu}, \tag{5.18}$$

which arises from the axial coupling of (5.17) leading to $g_{a_i\gamma\gamma} = \frac{\alpha}{2\pi v_i} \sum_{f,i} N_{cf} A^f_{ii} Q^2_f$ where N_{cf} is the color factor of the fermion f. For (5.15), we obtain,

$$g_{a_i\gamma\gamma} = \frac{4\alpha}{\pi v_i} = \frac{4\alpha}{\sqrt{2}\pi\varepsilon_i \Lambda} = \frac{2\alpha \tilde{N} \varepsilon_i^{\tilde{N}-4/2} \sqrt{|\lambda_i|}}{\sqrt{2}\pi m_{a_i}}, \tag{5.19}$$

where $i = 1-6$. The pseudoscalar a_7 does not couple to a pair of photons at leading-order since the field χ_7 is a singlet of the enforced $U(1)$ symmetry.

We show the masses of the SHVM ALPs in figure 5.14, which are overlaid on the limit plot provided by reference [232]. The ranges of the masses of the ALPs

forbidden by the limit plot provided by the reference [232] are given in exclusion table 5.1.

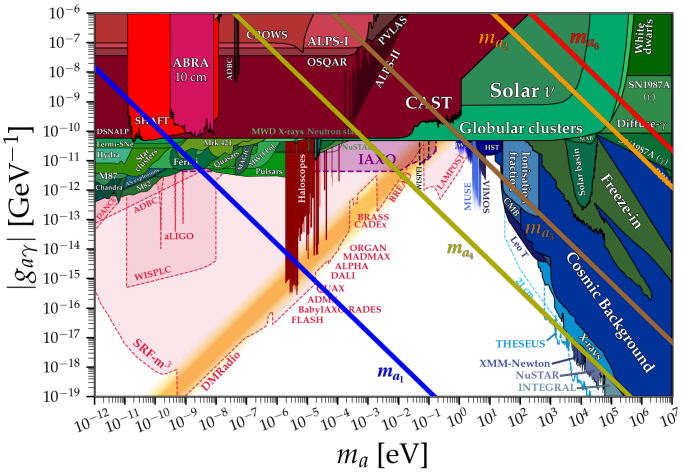

Fig. 5.14 The coupling $|g_{a_i\gamma\gamma}| = |g_{a\gamma\gamma}|$ and the ALPs masses $m_{a_i} = m_a$ of the SHVM for $\tilde{N} = 14$. The SHVM predictions are overlaid on the limit plot provided by reference [232]

a_i (Color)	m_{a_i} range (eV)	$g_{a_i\gamma\gamma}$ range (GeV^{-1})
a_1 (Blue)	$\approx (10^{-12} - 2\times 10^{-5})$	$\approx (8\times 10^{-16} - 1\times 10^{-8})$
a_2 (Yellow)	$\approx (12 - 10^7)$	$\approx (10^{-12} - 10^{-6})$
a_4 (Green)	$\approx (4\times 10^{-8} - 10^{-2})$ $\approx (10^3 - 3\times 10^5)$	$\approx (3\times 10^{-12} - 10^{-6})$ $\approx (10^{-19} - 3\times 10^{-17})$
a_5 (Brown)	$\approx (7\times 10^{-5} - 7)$ $\approx (24 - 10^7)$	$\approx (9\times 10^{-12} - 10^{-6})$ $\approx (6\times 10^{-18} - 3\times 10^{-12})$
a_6 (Red)	$\approx (2\times 10^2 - 10^7)$	$\approx (2\times 10^{-11} - 10^{-6})$

Table 5.1 Excluded ranges of m_{a_i} and corresponding ranges of the coupling $g_{a_i\gamma\gamma}$ for $\tilde{N} = 14$.

A large range of mass of the pseudoscalar a_4 is ruled out by the CAST data, and some part of the rest of the mass range will be probed by the IAXO and THESEUS experiments. We notice that a larger range of the mass of pseudoscalar a_1 is also

excluded by the CAST, SHAFT and Fermi data. WISPLC and several experiments will further probe a part of the mass range of pseudoscalar a_1. A sufficient part of the mass range of pseudoscalars a_1 and a_4 will remain beyond the reach of any present and future experiments.

5.4 Collider physics of the SHVM

In this section, we shall discuss the inclusive collider signatures of the SHVM. We use the `MSTW2008` PDF [200] for producing the production cross-sections of scalars h_i and pseudoscalar a_3 in various channels. As discussed earlier, the quark and lepton flavour bounds push the scale Λ to several TeV. This will suppress the signatures of the SHVM in collider physics. Therefore, we shall discuss the collider physics of the SHVM independent of the flavour bounds. This is possible in a scenario where the bounds on the SHVM from flavour physics are relaxed by some mechanism originating from the UV completion. For instance, the dark-technicolor paradigm discussed in appendix, which is a UV completion of the SHVM, may create the following soft-symmetry-breaking terms in the scalar potential due to the strong dynamics,

$$V_{\rm soft} = -\rho_i^2\ \chi_i^2 + \sigma_i\ \chi_i^3 + \text{H.c.}. \tag{5.20}$$

The scalar mass matrix, in this scenario, is approximately diagonal due to hierarchy in diagonal and off-diagonal terms. Therefore, we can take $s_i \approx h_i$ up to a good approximation, and the masses of scalars and pseudoscalars approximately are,

$$\begin{aligned} m_{h_i}^2 \approx& 16\varepsilon_i^2\Lambda^2\lambda_\chi + 6\sqrt{2}\varepsilon_i\Lambda\sigma_i, \\ m_{a_i}^2 \approx& 4\rho_i^2 - 9\sqrt{2}\varepsilon_i\Lambda\sigma_i. \end{aligned} \tag{5.21}$$

The masses of scalars and pseudo-scalars now depend on the mass parameters ρ_i and σ_i. This will result in a relaxation of the flavour limits on the scale Λ. A detailed flavour- and collider investigation of this scenario is beyond the scope of this paper. For collider investigation, we assume that the masses of scalars and pseudoscalars are generated by equation 5.20, and therefore are the free parameters. Moreover, we investigate a scenario where we have assumed $m_{a_i} < m_{h_i}$, and m_{a_3} is the heaviest pseudoscalar.

We investigate inclusive signatures $pp \to h_i/a_i \to f_i f_j/\gamma\gamma$ of the SHVM at the HL-LHC, HE-LHC, and a 100 TeV collider. We observe that due to the absence of interactions between the Higgs and χ fields in this work, there are no bounds on the masses of scalars and pseudo-scalars from the direct LHC searches [194]. Moreover, the decays of scalars and pseudoscalars to WW and ZZ bosons arise at one-loop level. Therefore, they are highly suppressed. ATLAS has placed a limit on masses above 300 GeV [195], and the CMS limit is 200 GeV [196]. The ATLAS has placed a bound above 200 GeV from the ATLAS [197], and that of the CMS is above 500 GeV from the CMS [198] in the di-photon channel searches.

The estimated reaches ($\sigma \times BR$) of the HL-LHC, HE-LHC and a 100 TeV hadron collider in different inclusive channels for a heavy and a light pseudoscalar are taken from reference [16], and are given in tables 5.2 and 5.3. In general, inclusive decay modes of the SHVM, accessible to the HL-LHC, the HE-LHC and a 100 TeV collider, are marked by the box ($\square$).

	HL-LHC [14 TeV, 3 ab^{-1}]		HE-LHC [27 TeV, 15 ab^{-1}]		100 TeV, 30 ab^{-1}	
m_a [GeV]	20	60	20	60	20	60
$\tau\tau$ [pb]		0.9		0.5		0.6
$\gamma\gamma$ [pb]	1.3	1.5	0.7	0.8	0.8	0.9

Table 5.3 Estimated reach ($\sigma \times BR$) of the HL-LHC, HE-LHC and a 100 TeV collider for low mass pseudoscalar (m_a) in inclusive production channels.

m_a [GeV]	HL-LHC [14 TeV, 3 ab^{-1}] 500	1000	HE-LHC [27 TeV, 15 ab^{-1}] 500	1000	100 TeV, 30 ab^{-1} 500	1000
$\tau\tau$ [pb]	$7\cdot10^{-3}$	$1\cdot10^{-3}$	$4\cdot10^{-3}$	$7\cdot10^{-4}$	$5\cdot10^{-3}$	$8\cdot10^{-4}$
ee, $\mu\mu$ [pb]	$2\cdot10^{-4}$	$4\cdot10^{-5}$	$1\cdot10^{-4}$	$3\cdot10^{-5}$	$1\cdot10^{-4}$	$3\cdot10^{-5}$
μe [pb]	$9\cdot10^{-4}$	$7\cdot10^{-5}$	$7\cdot10^{-4}$	$5\cdot10^{-5}$	$1\cdot10^{-3}$	$1\cdot10^{-4}$
$\mu\tau$ [pb]	$2\cdot10^{-3}$	$2\cdot10^{-4}$	$1\cdot10^{-3}$	$2\cdot10^{-4}$	$2\cdot10^{-3}$	$3\cdot10^{-4}$
$e\tau$ [pb]	$1\cdot10^{-3}$	$2\cdot10^{-4}$	$8\cdot10^{-4}$	$2\cdot10^{-4}$	$1\cdot10^{-3}$	$3\cdot10^{-4}$
$b\bar{b}$ [pb]		$9\cdot10^{-3}$		$5\cdot10^{-3}$		$7\cdot10^{-3}$
$\gamma\gamma$ [pb]	$1\cdot10^{-4}$	$2\cdot10^{-5}$	$6\cdot10^{-5}$	$1\cdot10^{-5}$	$7\cdot10^{-5}$	$1\cdot10^{-5}$
$t\bar{t}$ [pb]	4	$5\cdot10^{-2}$	3	$4\cdot10^{-2}$	8	0.1

Table 5.2 Estimated reach ($\sigma \times BR$) of the HL-LHC, HE-LHC and a 100 TeV hadron collider for a high mass pseudoscalar (m_a) in inclusive production channels.

5.4.1 A unique signature of the SHVM and 95.4 GeV excess

A distinct signature of the SHVM, which keeps the SHVM apart from any other flavour models in the literature, is the decay of the pseudoscalar a_3. The pseudoscalar a_3 couples to only $t\bar{t}$ pair. Therefore, the only decay modes available for this particle are $\gamma\gamma$, gg, and $t\bar{t}$ pairs depending on the kinematics. Thus, the pseudoscalar a_3 is a unique particle among pseudoscalars a_i.

In this section, we study the production and decays of pseudoscalar a_3 at the HL-LHC, HE-LHC, and a 100 TeV collider such as FCC-hh. We show the branching ratios of the pseudoscalar a_3 in figure 5.15, and the production cross sections for the $\gamma\gamma$ and $t\bar{t}$ modes, as a function of the mass of the pseudoscalar a_3, are shown in figure 5.16 for the scale $\Lambda = 500$ GeV.

We show in tables 5.4 and 5.5, our benchmark predictions for the heavy and light pseudoscalar a_3 for the scale $\Lambda = 500$ GeV. We observe that the HL-LHC will not be able to search heavy masses of pseudoscalar a_3. The HE-LHC and a 100 TeV collider can probe the pseudoscalar a_3 in $t\bar{t}$ mode. The light masses of pseudoscalar a_3 are beyond the reach of any colliders.

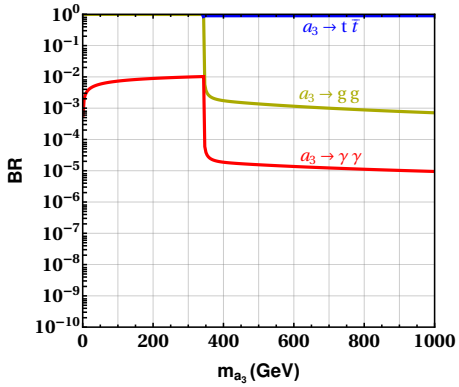

Fig. 5.15 Branching ratios of various possible decay modes of the pseudoscalar a_3.

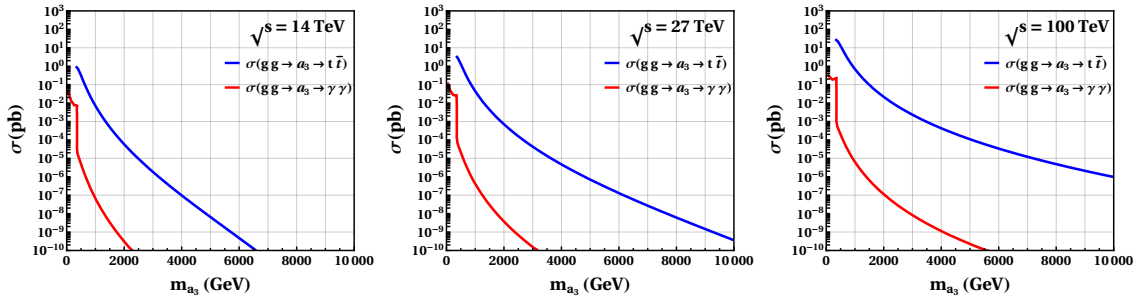

(a) (b) (c)

Fig. 5.16 Cross-section ($\sigma \times BR$) for the processes $pp \to a_3 \to t\bar{t}$ and $pp \to a_3 \to \gamma\gamma$ as functions of the pseudoscalar mass m_{a_3} are shown in figure 5.16a for the 14 TeV HL-LHC, figure 5.16b for the 27 TeV HE-LHC, and in figure 5.16c for a 100 TeV collider, where we have set the scale $\Lambda = 500$ GeV.

	HL-LHC [14 TeV, 3 ab^{-1}]		HE-LHC [27 TeV, 15 ab^{-1}]		100 TeV, 30 ab^{-1}	
m_{a_3} [GeV]	500	1000	500	1000	500	1000
$\gamma\gamma$ [pb]	$4 \cdot 10^{-6}$	$6 \cdot 10^{-8}$	$2 \cdot 10^{-5}$	$4 \cdot 10^{-7}$	$\boxed{2 \cdot 10^{-4}}$	$6 \cdot 10^{-6}$
$t\bar{t}$ [pb]	0.29	$7 \cdot 10^{-3}$	1.2	$\boxed{4 \cdot 10^{-2}}$	$\boxed{12.6}$	0.68

Table 5.4 Benchmark ($\sigma \times BR$) for higher mass of the pseudoscalar m_{a_3}, where $\Lambda = 500$ GeV.

	HL-LHC [14 TeV, 3 ab^{-1}]		HE-LHC [27 TeV, 15 ab^{-1}]		100 TeV, 30 ab^{-1}	
m_a [GeV]	20	60	20	60	20	60
$\gamma\gamma$ [pb]	$7 \cdot 10^{-2}$	$4 \cdot 10^{-2}$	0.14	$8 \cdot 10^{-2}$	0.44	0.37

Table 5.5 Benchmark ($\sigma \times BR$) for low pseudoscalar mass m_{a_3}, where $\Lambda = 500$ GeV.

We now discuss a low-mass di-photon excess reported by the CMS collaboration at $m_{\gamma\gamma} = 95.4$ GeV with a local significance of 2.9σ [233]. This excess is also supported by the similar results reported by the ATLAS collaboration with a local significance of 1.7σ [234]. The combined signal strength can be written as [235],

$$\mu_{\gamma\gamma}^{exp} = \mu_{\gamma\gamma}^{ATLAS+CMS} = \frac{\sigma(pp \to \phi \to \gamma\gamma)}{\sigma_{SM}(pp \to h_{95.4}^{SM} \to \gamma\gamma)} = 0.24^{+0.09}_{-0.08}, \tag{5.22}$$

with a local significance of 3.1σ. We notice that ϕ represents a non-SM scalar with a mass of 95.4 GeV, and the scalar $h_{95.4}^{SM}$ shows a SM-like Higgs with the same mass. There are numerous explanation to this observation [235]-[293].

In the SHVM, this excess can be addressed through the pseudoscalar a_3, which is insensitive to the flavour bounds. We address this excess in the scenario where $m_{a_i} << m_{h_i}$ and pseudoscalar a_3 is the heaviest pseudoscalar. In this case, the scale Λ can be as low as the electroweak scale since the masses of scalar h_i can be treated as free parameters.

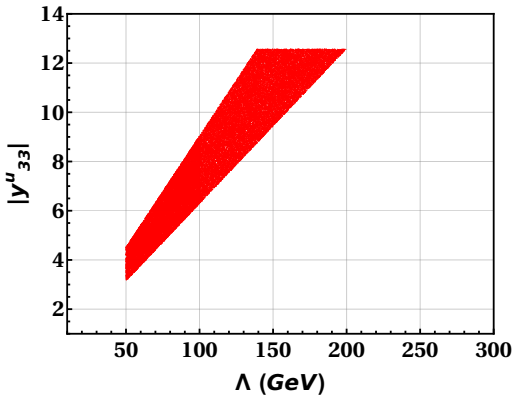

Fig. 5.17 Allowed values of y_{33}^{u} and Λ for a_3 to address the di-photon excess at $m_{\gamma\gamma}$ = 95.4 GeV.

There are only two free parameters $|y_{33}^{u}|$ and Λ in producing the 95.4 GeV excess. This is because the coupling of the pseudoscalar a_3 to $t\bar{t}$ pair is independent of the

parameter ε_3. We show the variation of the $|y^u_{33}|$ and Λ, which can produce the 95.4 excess, in figure 5.17.

5.4.2 Signatures of scalars

We now investigate the decay profiles and collider signatures emerging through the scalars h_i of the SHVM assuming the scale $\Lambda = 500$ GeV.

Scalar h_1

The dominant couplings of scalar h_1 are with the pairs e^-e^+ and $u\bar{u}$. We show the branching ratios of scalar h_1 in figure 5.18. The production cross-sections for inclusive modes e^-e^+ and $\gamma\gamma$ are shown in figure 5.19.

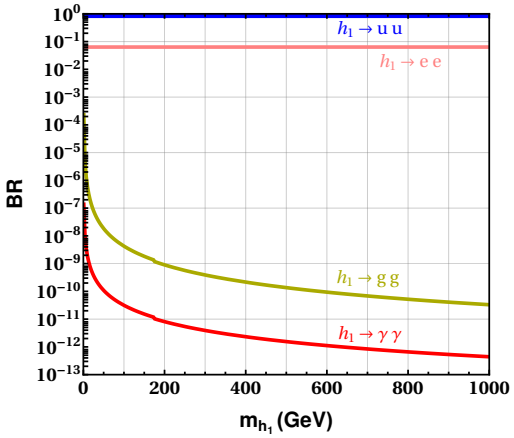

Fig. 5.18 The branching ratio of various possible decay modes of the scalar h_1, assuming $\Lambda = 500$ GeV.

We show the benchmark predictions for the scalar h_1 for the heavy and light masses at the scale $\Lambda = 500$ GeV in tables 5.6 and 5.7. We notice that only e^-e^+ production channel is accessible to the HL-LHC, the HE-LHC, and a 100 TeV collider in the case of a heavy mass.

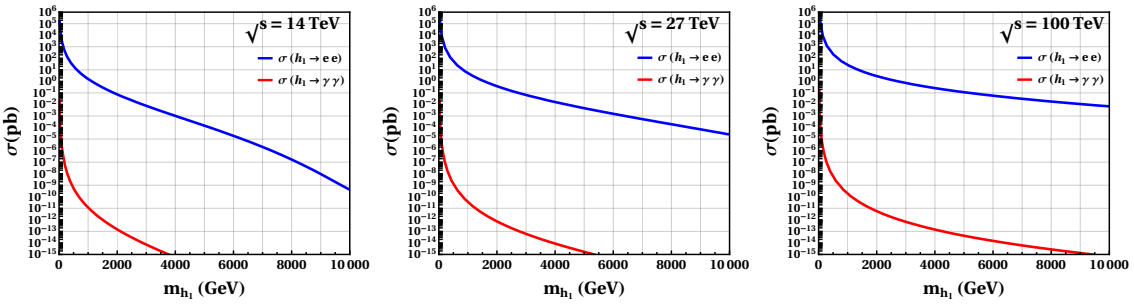

(a) (b) (c)

Fig. 5.19 Cross-section ($\sigma \times BR$) for the processes $pp \to h_1 \to ee$ and $pp \to h_1 \to \gamma\gamma$ as functions of the scalar mass m_{h_1} are shown in figure 5.19a for the 14 TeV HL-LHC, figure 5.19b for the 27 TeV HE-LHC, and in figure 5.19c for a 100 TeV collider, where the scale $\Lambda = 500$ GeV.

	HL-LHC [14 TeV, 3 ab^{-1}]		HE-LHC [27 TeV, 15 ab^{-1}]		100 TeV, 30 ab^{-1}	
m_{h_1} [GeV]	500	1000	500	1000	500	1000
$e\bar{e}$ [pb]	$\boxed{21.2}$	$\boxed{1.7}$	$\boxed{49.7}$	$\boxed{4.9}$	$\boxed{214.7}$	$\boxed{26.7}$
$\gamma\gamma$ [pb]	$5 \cdot 10^{-10}$	$1 \cdot 10^{-11}$	$1 \cdot 10^{-9}$	$3 \cdot 10^{-11}$	$5 \cdot 10^{-9}$	$2 \cdot 10^{-10}$

Table 5.6 Benchmark ($\sigma \times BR$) for higher values of the scalar mass m_{h_1}, where $\Lambda = 500$ GeV.

	HL-LHC [14 TeV, 3 ab^{-1}]		HE-LHC [27 TeV, 15 ab^{-1}]		100 TeV, 30 ab^{-1}	
m_{h_1} [GeV]	20	60	20	60	20	60
$\gamma\gamma$ [pb]	$2 \cdot 10^{-3}$	$1 \cdot 10^{-5}$	$3 \cdot 10^{-3}$	$3 \cdot 10^{-5}$	$6 \cdot 10^{-3}$	$8 \cdot 10^{-5}$

Table 5.7 Benchmark ($\sigma \times BR$) for low values of the scalar mass m_{h_1}, where $\Lambda = 500$ GeV.

Scalar h_2

The scalar h_2 couples dominantly with the pairs $\tau^-\tau^+$, $c\bar{c}$, and $t\bar{u}$. We show the branching ratios of scalar h_2 in figure 5.20. The production cross-sections for inclusive modes $\tau^-\tau^+$, $\mu^+\tau^-$, and $\gamma\gamma$ at the HL-LHC, the HE-LHC, and a 100 TeV collider are shown in figure 5.21.

The benchmark predictions for the scalar h_2 are shown in tables 5.8 and 5.9 for the heavy and light masses at the scale $\Lambda = 500$ GeV. The $\tau\tau$ production channel is accessible to the HL-LHC, the HE-LHC and a 100 TeV collider for heavy as well as light masses. The $\mu^+\tau^-$ mode is within the reach of all colliders only for a heavy mass.

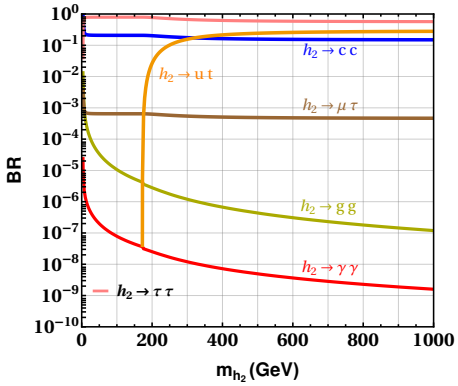

Fig. 5.20 The branching ratio of various possible decay modes of the scalar h_2, with $\Lambda = 500$ GeV.

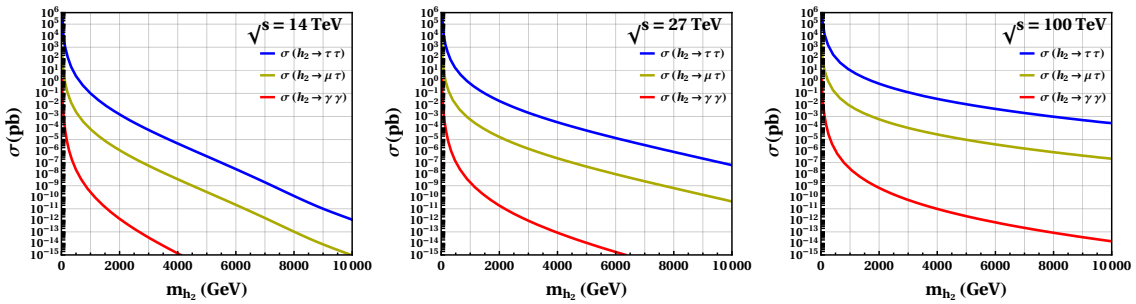

(a) (b) (c)

Fig. 5.21 Cross-section ($\sigma \times BR$) for the processes $pp \to h_2 \to \tau\tau$, $pp \to h_2 \to \mu\tau$, and $pp \to h_2 \to \gamma\gamma$ as functions of the scalar mass m_{h_2} are shown in figure 5.21a for the 14 TeV HL-LHC, 5.21b for the 27 TeV HE-LHC, and in figure 5.21c for a 100 TeV collider, where the scale $\Lambda = 500$ GeV.

	HL-LHC [14 TeV, 3 ab^{-1}]		HE-LHC [27 TeV, 15 ab^{-1}]		100 TeV, 30 ab^{-1}	
m_{h_2} [GeV]	500	1000	500	1000	500	1000
$\tau\tau$ [pb]	$\boxed{2.9}$	$\boxed{0.1}$	$\boxed{12.5}$	$\boxed{0.7}$	$\boxed{116}$	$\boxed{10.1}$
$\mu\tau$ [pb]	$\boxed{2.4\cdot10^{-3}}$	$8.1\cdot10^{-5}$	$\boxed{1\cdot10^{-2}}$	$\boxed{5.4\cdot10^{-4}}$	$\boxed{9.5\cdot10^{-2}}$	$\boxed{8.2\cdot10^{-3}}$
$\gamma\gamma$ [pb]	$2.4\cdot10^{-8}$	$2.7\cdot10^{-10}$	$1\cdot10^{-7}$	$1.8\cdot10^{-9}$	$9.6\cdot10^{-7}$	$2.8\cdot10^{-8}$

Table 5.8 Benchmark ($\sigma \times BR$) for higher values of the scalar mass m_{h_2}, where $\Lambda = 500$ GeV.

	HL-LHC [14 TeV, 3 ab^{-1}]		HE-LHC [27 TeV, 15 ab^{-1}]		100 TeV, 30 ab^{-1}	
m_{h_2} [GeV]	20	60	20	60	20	60
$\tau\tau$ [pb]	$1.4\cdot10^{5}$	$\boxed{7.8\cdot10^{3}}$	$2.7\cdot10^{5}$	$\boxed{1.7\cdot10^{4}}$	$8.4\cdot10^{5}$	$\boxed{7\cdot10^{4}}$
$\gamma\gamma$ [pb]	0.12	$1.5\cdot10^{-3}$	0.22	$3.4\cdot10^{-3}$	0.66	$1.4\cdot10^{-2}$

Table 5.9 Benchmark ($\sigma \times BR$) for low values of the scalar mass m_{h_2}, where $\Lambda = 500$ GeV.

Scalar h_3

The scalar h_3 primarily interacts with the $t\bar{t}$ pair at the tree level. Figure 5.22 shows the branching ratios for various possible decay modes of h_3. While the $t\bar{t}$ channel dominates, the loop-induced decay modes into gg and $\gamma\gamma$ are also significant compared to other scalars, which is due to the contribution of the top quark in the loop. In figure 5.23, we present the production cross-section for the inclusive modes $t\bar{t}$ and $\gamma\gamma$ at the HL-LHC, HE-LHC, and a 100 TeV collider.

Benchmark values for the production cross-section at the scale $\Lambda = 500$ GeV are summarized in Tables 5.10 and 5.11, corresponding to the heavy and light mass of the scalar h_3, respectively. The $t\bar{t}$ channel is evidently beyond the reach of the HL-LHC. However, this mode becomes accessible at the HE-LHC and a 100 TeV collider, as marked by the box ($\boxed{\ }$) in the tables. The di-photon $\gamma\gamma$ mode remains insensitive to any of the three future colliders in both the heavy and light mass scenarios.

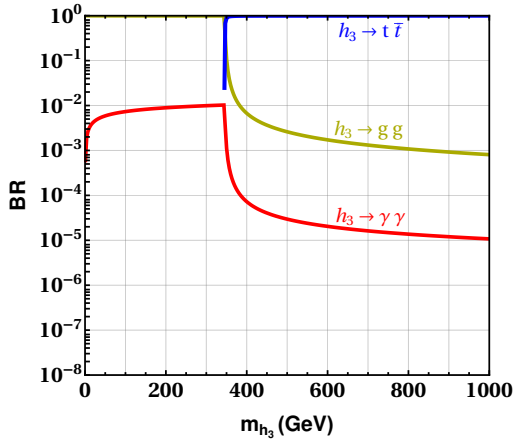

Fig. 5.22 The branching ratio of various possible decay modes of the scalar h_3, assuming $\Lambda = 500$ GeV.

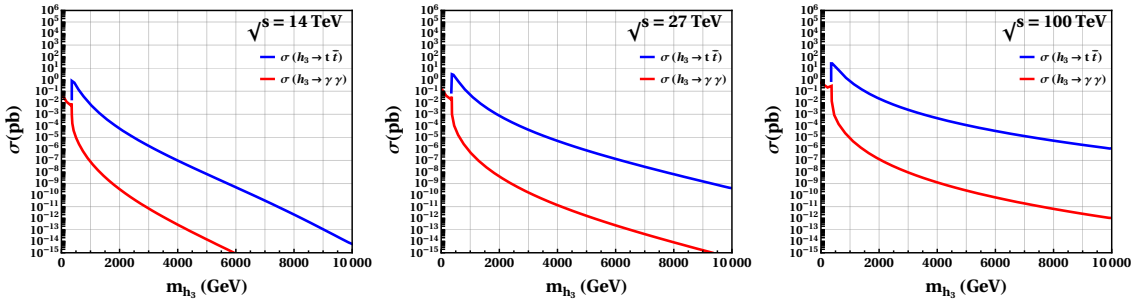

(a) (b) (c)

Fig. 5.23 Cross-section ($\sigma \times BR$) for the processes $pp \to h_3 \to t\bar{t}$ and $pp \to h_3 \to \gamma\gamma$ as functions of the scalar mass m_{h_3} are shown in figure 5.23a for the 14 TeV HL-LHC, figure 5.23b for the 27 TeV HE-LHC, and in figure 5.23c a 100 TeV collider, assuming the scale $\Lambda = 500$ GeV.

	HL-LHC [14 TeV, 3 ab^{-1}]		HE-LHC [27 TeV, 15 ab^{-1}]		100 TeV, 30 ab^{-1}	
m_{h_3} [GeV]	500	1000	500	1000	500	1000
$t\bar{t}$ [pb]	0.31	$7.2 \cdot 10^{-3}$	1.32	$\boxed{4.5 \cdot 10^{-2}}$	$\boxed{13.4}$	$\boxed{0.72}$
$\gamma\gamma$ [pb]	$9 \cdot 10^{-6}$	$8 \cdot 10^{-8}$	$4 \cdot 10^{-5}$	$5 \cdot 10^{-7}$	$4 \cdot 10^{-4}$	$8 \cdot 10^{-6}$

Table 5.10 Benchmark ($\sigma \times BR$) for higher values of the scalar mass m_{h_3}, where $\Lambda = 500$ GeV.

Scalar h_4

The various possible decay channels of the scalar h_4 are represented in figure 5.24, where it dominantly decays to the $d\bar{b}$, $d\bar{s}$, $d\bar{d}$, and $e\bar{\mu}$ pairs. The production

m_{h_3} [GeV]	HL-LHC [14 TeV, 3 ab^{-1}] 20	60	HE-LHC [27 TeV, 15 ab^{-1}] 20	60	100 TeV, 30 ab^{-1} 20	60
$\gamma\gamma$ [pb]	$8\cdot10^{-2}$	$4\cdot10^{-2}$	0.15	$9\cdot10^{-2}$	0.47	0.39

Table 5.11 Benchmark ($\sigma\times BR$) for low values of the scalar mass m_{h_3}, where $\Lambda = 500$ GeV.

cross-sections of the scalar h_4 for the inclusive channels $e\bar{\mu}$ and $\gamma\gamma$ are shown in figure 5.25 at the HL-LHC, HE-LHC, and a 100 TeV collider.

The benchmark predictions of the production cross-sections at the scale $\Lambda = 500$ GeV, through the inclusive channels $e\bar{\mu}$ and $\gamma\gamma$, are given in table 5.12 for the case when the scalar h_4 is heavy, and in table 5.13 for a light mass of scalar h_4. The inclusive channel $e\bar{\mu}$ is within the reach of HL-LHC, HE-LHC, and a 100 TeV collider for a heavy mass of scalar m_{h_4}, while the di-photon $\gamma\gamma$ channel remains beyond the reach of any of the three future colliders.

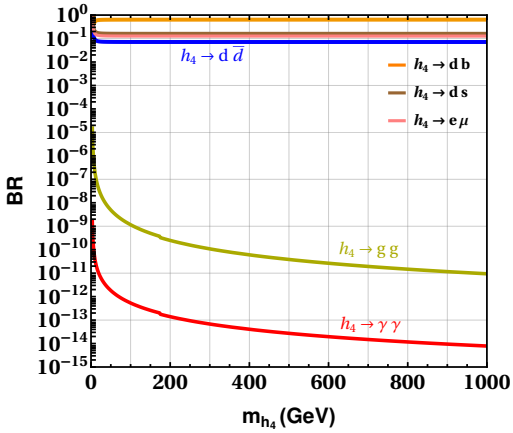

Fig. 5.24 The branching ratio of various possible decay modes of the scalar h_4, assuming $\Lambda = 500$ GeV.

Scalar h_5

We now examine the signatures of the scalar h_5. Its potential decay modes include $s\bar{s}$, $s\bar{b}$, $s\bar{d}$ as well as the leptonic channels $\mu\bar{\mu}$, and $e\bar{\tau}$. Additionally, there are

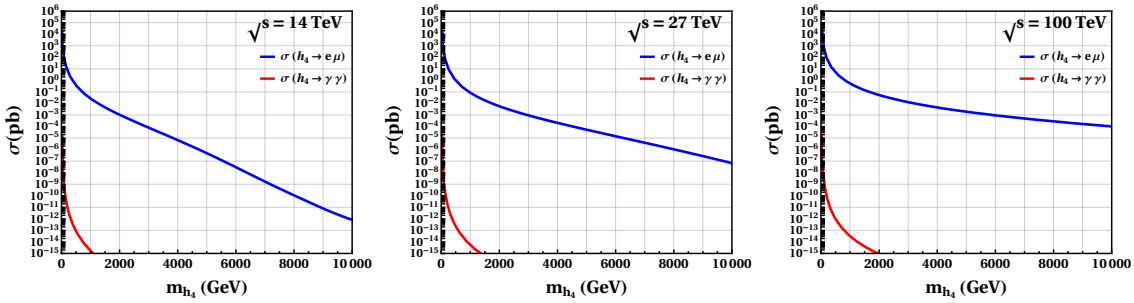

(a) (b) (c)

Fig. 5.25 Cross-section ($\sigma \times BR$) for the processes $pp \to h_4 \to e\mu$ and $pp \to h_4 \to \gamma\gamma$ as functions of the scalar mass m_{h_4} are shown in figure 5.25a for the 14 TeV HL-LHC, figure 5.25b for the 27 TeV HE-LHC, and in figure 5.25c for a 100 TeV collider, where we have taken the scale $\Lambda = 500$ GeV.

	HL-LHC [14 TeV, 3 ab^{-1}]		HE-LHC [27 TeV, 15 ab^{-1}]		100 TeV, 30 ab^{-1}	
m_{h_4} [GeV]	500	1000	500	1000	500	1000
$e\mu$ [pb]	$\boxed{0.37}$	$\boxed{2.7 \cdot 10^{-2}}$	$\boxed{0.93}$	$\boxed{9 \cdot 10^{-2}}$	$\boxed{4.51}$	$\boxed{0.53}$
$\gamma\gamma$ [pb]	$8 \cdot 10^{-14}$	$2 \cdot 10^{-15}$	$2 \cdot 10^{-13}$	$5 \cdot 10^{-15}$	$9 \cdot 10^{-13}$	$3 \cdot 10^{-14}$

Table 5.12 Benchmark ($\sigma \times BR$) for higher values of the scalar mass m_{h_4}, where $\Lambda = 500$ GeV.

	HL-LHC [14 TeV, 3 ab^{-1}]		HE-LHC [27 TeV, 15 ab^{-1}]		100 TeV, 30 ab^{-1}	
m_{h_4} [GeV]	20	60	20	60	20	60
$\gamma\gamma$ [pb]	$3 \cdot 10^{-7}$	$3 \cdot 10^{-9}$	$5 \cdot 10^{-7}$	$5 \cdot 10^{-9}$	$1 \cdot 10^{-6}$	$2 \cdot 10^{-8}$

Table 5.13 Benchmark ($\sigma \times BR$) for low values of the scalar mass m_{h_4}, where $\Lambda = 500$ GeV.

loop-induced modes gg and $\gamma\gamma$, which are significantly suppressed in comparison. The branching fractions of these decay channels as a function of the mass of the scalar h_5, are illustrated in the figure 5.26. The production cross-sections of the scalar h_5, as a function of the scalar mass m_{h_5}, are shown in figure 5.27 at the HL-LHC, HE-LHC, and a 100 TeV collider.

The benchmark predictions for the production cross-sections at the HL-LHC, HE-LHC, and a 100 TeV collider for the heavy and light scalar mass m_{h_5} are listed in the tables 5.14 and 5.15, respectively, where we set the scale $\Lambda = 500$ GeV. For heavy scalar mass m_{h_5}, the inclusive channels $\mu\bar{\mu}$ and $e\bar{\tau}$ are accessible to HL-LHC, HE-LHC, as well as a 100 TeV collider. In contrast, the di-photon $\gamma\gamma$ channel remains insensitive to the HL-LHC, HE-LHC, and a 100 TeV collider, regardless of whether the scalar h_5 is heavy or light.

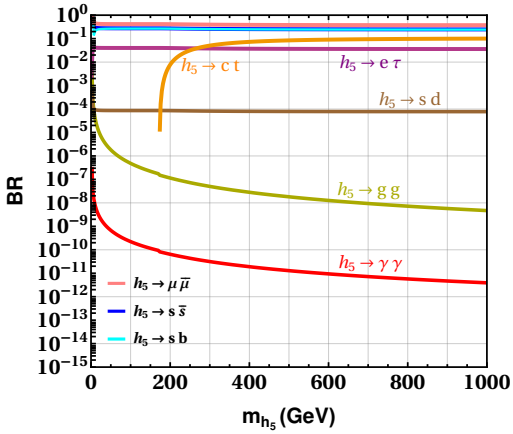

Fig. 5.26 The branching ratio of various possible decay modes of the scalar h_5, with the scale $\Lambda = 500$ GeV.

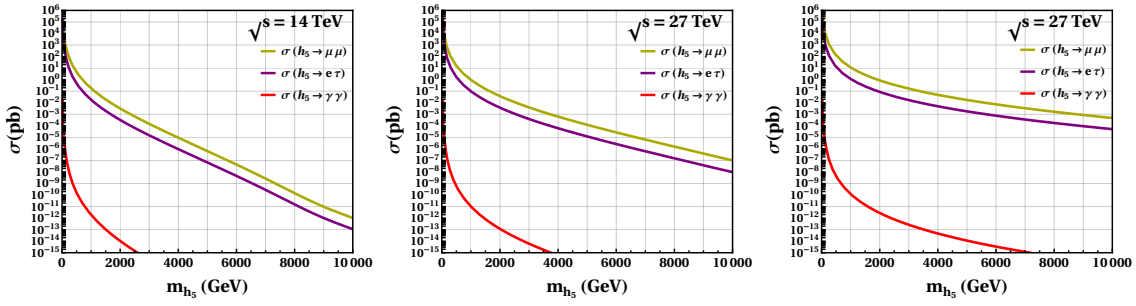

(a) (b) (c)

Fig. 5.27 Cross-section ($\sigma \times BR$) for the processes $pp \to h_5 \to \mu\mu$, $pp \to h_5 \to e\tau$, and $pp \to h_5 \to \gamma\gamma$ as functions of the scalar mass m_{h_5}, are shown in figure 5.27a for the 14 TeV HL-LHC, figure 5.27b for the 27 TeV HE-LHC, and in figure 5.27c for a 100 TeV collider, where we have set the scale $\Lambda = 500$ GeV.

	HL-LHC [14 TeV, 3 ab^{-1}]		HE-LHC [27 TeV, 15 ab^{-1}]		100 TeV, 30 ab^{-1}	
m_{h_5} [GeV]	500	1000	500	1000	500	1000
$\mu\mu$ [pb]	$\boxed{4.5}$	$\boxed{0.2}$	$\boxed{16.4}$	$\boxed{1.0}$	$\boxed{124.9}$	$\boxed{11.9}$
$e\tau$ [pb]	$\boxed{0.43}$	$\boxed{1.8\cdot10^{-2}}$	$\boxed{1.6}$	$\boxed{0.1}$	$\boxed{12}$	$\boxed{1.2}$
$\gamma\gamma$ [pb]	$1\cdot10^{-10}$	$2\cdot10^{-12}$	$5\cdot10^{-10}$	$1\cdot10^{-11}$	$4\cdot10^{-9}$	$1\cdot10^{-10}$

Table 5.14 Benchmark ($\sigma \times BR$) for higher values of the scalar mass m_{h_5}, where $\Lambda = 500$ GeV.

	HL-LHC [14 TeV, 3 ab^{-1}]		HE-LHC [27 TeV, 15 ab^{-1}]		100 TeV, 30 ab^{-1}	
m_{h_5} [GeV]	20	60	20	60	20	60
$\gamma\gamma$ [pb]	$9\cdot10^{-4}$	$9\cdot10^{-6}$	$2\cdot10^{-3}$	$2\cdot10^{-5}$	$5\cdot10^{-3}$	$7\cdot10^{-5}$

Table 5.15 Benchmark ($\sigma \times BR$) for low values of the scalar mass m_{h_5}, where $\Lambda = 500$ GeV.

Scalar h_6

The scalar h_6 prominently couples to the $b\bar{b}$, $b\bar{s}$, $b\bar{d}$, and $t\bar{c}$ pairs. The branching fractions of the scalar h_6 into these decay modes including the loop-induced gg and $\gamma\gamma$ channels, are shown in figure 5.28. It is evident that the decay into $b\bar{b}$ pairs dominates. The $t\bar{c}$ decay mode, which shows up at the top-threshold is also notable, but remains less significant than the $b\bar{b}$. The production cross-sections of the scalar h_6 for the inclusive channels $b\bar{b}$ and $\gamma\gamma$ at the HL-LHC, HE-LHC, and a 100 TeV collider, are shown in figure 5.29.

The benchmark predictions for the production cross-sections of the scalar h_6 at the scale $\Lambda = 500$ GeV, are given in tables 5.16 and 5.17, corresponding to the heavy and light mass scenarios of h_6, respectively. For a heavy scalar mass m_{h_6}, the inclusive $b\bar{b}$ channel is accessible at the HL-LHC, HE-LHC, and a 100 TeV collider. The di-photon $\gamma\gamma$ channel remains beyond the reach of all the three future colliders for the heavy scalar h_6. However, for a sufficiently light scalar mass m_{h_6}, the $\gamma\gamma$

channel, which was previously insensitive to other scalars, becomes accessible to both the HE-LHC and a 100 TeV collider, setting it apart from other scalars.

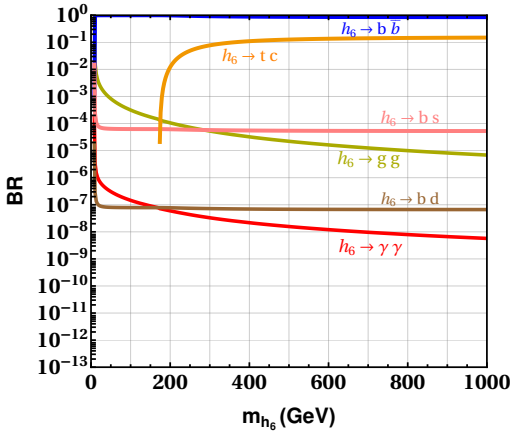

Fig. 5.28 The branching ratio of various possible decay modes of the scalar h_6, assuming the scale $\Lambda = 500$ GeV.

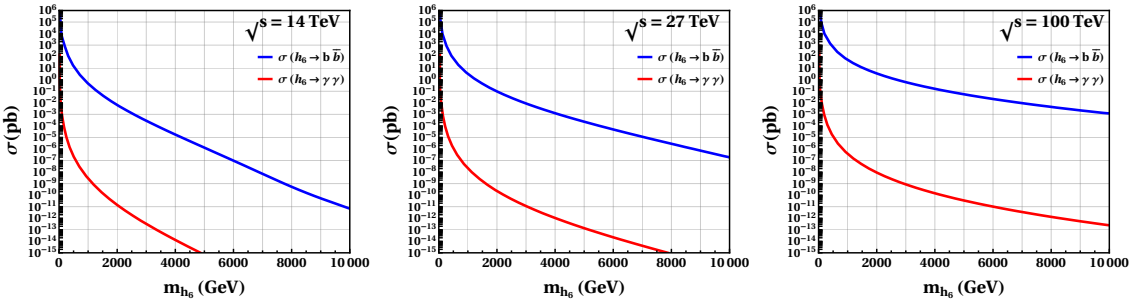

(a) (b) (c)

Fig. 5.29 Cross-section ($\sigma \times BR$) for the processes $pp \to h_6 \to b\bar{b}$ and $pp \to h_6 \to \gamma\gamma$ as functions of the scalar mass m_{h_6}, are shown in figure 5.29a for the 14 TeV HL-LHC, figure 5.29b for the 27 TeV HE-LHC, and in figure 5.29c for a 100 TeV collider, where we have set the scale $\Lambda = 500$ GeV.

	HL-LHC [14 TeV, 3 ab^{-1}]		HE-LHC [27 TeV, 15 ab^{-1}]		100 TeV, 30 ab^{-1}	
m_{h_6} [GeV]	500	1000	500	1000	500	1000
$b\bar{b}$ [pb]	13.1	$\boxed{0.44}$	60.7	$\boxed{3.2}$	647.6	$\boxed{56.5}$
$\gamma\gamma$ [pb]	$2\cdot10^{-7}$	$3\cdot10^{-9}$	$1\cdot10^{-6}$	$2\cdot10^{-8}$	$1\cdot10^{-5}$	$4\cdot10^{-7}$

Table 5.16 Benchmark ($\sigma \times BR$) for higher values of the scalar mass m_{h_6}, where $\Lambda = 500$ GeV.

	HL-LHC [14 TeV, 3 ab^{-1}]		HE-LHC [27 TeV, 15 ab^{-1}]		100 TeV, 30 ab^{-1}	
m_{h_6} [GeV]	20	60	20	60	20	60
$\gamma\gamma$ [pb]	0.47	$8\cdot10^{-3}$	$\boxed{0.93}$	$2\cdot10^{-2}$	$\boxed{3.06}$	$8\cdot10^{-2}$

Table 5.17 Benchmark ($\sigma \times BR$) for low values of the scalar mass m_{h_6}, where $\Lambda = 500$ GeV.

Scalar h_7

The couplings of scalar h_7 to a pair of fermions are extremely small. For instance, the largest coupling of scalar h_7 is to the pairs of $u\bar{u}$ and ee, and is of the order $10^{-5}v/\sqrt{2}\Lambda$. Therefore, it does not show any appreciable signature in collider physics.